

Cite this: *Mater. Adv.*, 2025,  
6, 6454

## Cold sintered TiO<sub>2</sub>–Ti<sub>3</sub>C<sub>2</sub>T<sub>x</sub> MXene nanocomposites for supercapacitor electrode materials†

Abdul Hamid Rumman,<sup>a</sup> Saimon Mahmud,<sup>a</sup> Nishat Tasnim Mim,<sup>a</sup> Janifa Akter,<sup>a</sup> Ananya Roy,<sup>a</sup> Ahsior Rahman Nirjhar,<sup>a</sup> Md. Nazmul Ahsan Dipon,<sup>a</sup> Md. Shofiqul Islam,<sup>b</sup> Md Abdul Gafur,<sup>b</sup> Aninda Nafis Ahmed\*<sup>b</sup> and Kazi Md. Shorowordi<sup>b</sup>

MXene-based materials exhibit unique electrochemical properties due to their 2D layered structure with high surface areas, making them ideal candidates for electrode materials in advanced electrochemical energy storage systems. The capacitive properties of Ti<sub>3</sub>C<sub>2</sub>T<sub>x</sub> MXenes (T<sub>x</sub> denotes the surface terminator group, such as –F, –OH, and =O) can be enhanced by decorating surface layers with transition metal oxides, such as TiO<sub>2</sub>. Conventional *in situ* synthesis methods lack precise control over the TiO<sub>2</sub> content within the MXene structure. In this study, a contemporary cold sintering process (CSP) was employed to fabricate the TiO<sub>2</sub>–Ti<sub>3</sub>C<sub>2</sub>T<sub>x</sub> nanocomposite, enabling a controlled amount of TiO<sub>2</sub> particle addition into the MXene matrix. Consequently, it provided a means to correlate the electrochemical performance of the nanocomposites with the TiO<sub>2</sub> content. Through the CSP, the nanocomposites were fabricated at low temperature (150 °C) and pressure (150 MPa) assisted by a transient liquid, achieving high relative density (> 85%). The electrochemical performance analysis revealed an increase in specific capacitance with increasing TiO<sub>2</sub> content, reaching up to 117 F g<sup>–1</sup> for (40 wt%) TiO<sub>2</sub>/MXene at a 10 mV s<sup>–1</sup> scan rate surpassing that of the pristine MXene (55.29 F g<sup>–1</sup>). Additionally, the charge transfer resistance substantially declined from 4.01 Ω cm<sup>2</sup> for the pristine MXene to as low as 0.51 Ω cm<sup>2</sup> for (40 wt%) TiO<sub>2</sub>/MXene. Surprisingly, the nanocomposite samples demonstrated more than a 200% increase in the specific capacitance after 1000 charging–discharging cycles at 1.5 A g<sup>–1</sup>, attributed to the ion intercalation and surface terminator group (T<sub>x</sub>) alteration in MXenes. Overall, this study highlights the application of the CSP as a valuable tool for precisely tailoring the electrochemical properties of TiO<sub>2</sub>–Ti<sub>3</sub>C<sub>2</sub>T<sub>x</sub> MXene nanocomposites.

Received 8th December 2024,  
Accepted 24th July 2025

DOI: 10.1039/d4ma01212g

rsc.li/materials-advances

## 1. Introduction

The proliferating usage of electric vehicles, electronic devices, and smart grid technologies necessitate advanced energy storage devices offering high energy density, rapid charging–discharging rates, and prolonged cycling stability. Supercapacitors (SCs), with the capability of rapid charge and discharge, are utilized in applications requiring rapid bursts of energy, such as regenerative braking systems and power backup systems. Nevertheless, owing

to the superior range of energy and power densities compared to other devices, supercapacitors have become a viable option for enhancing energy storage capabilities.<sup>1</sup> Supercapacitors (SCs) can be classified into three major categories based on their energy storage mechanisms: electrochemical double-layer capacitors (EDLCs), pseudo capacitors (PCs), and hybrid capacitors (HCs). EDLCs, which are primarily made of carbon-based materials, store energy by ion adsorption–desorption at the electrode/electrolyte interface.<sup>2–5</sup> PCs use electroactive materials such as metal oxides, metal-doped carbon, and conductive polymers to store energy through reversible faradaic redox processes.<sup>6</sup> Contemporary research is more focused on pseudocapacitors (PCs) as the charge storage mechanism involves a faradaic redox process capable of delivering higher capacitance values and offering a vast range of choices on materials, such as metal oxides, polymers, and composites.<sup>7</sup> MXenes are 2D layered materials that have significant potential in energy storage applications. It is represented by

<sup>a</sup> Department of Materials and Metallurgical Engineering (MME), Bangladesh University of Engineering and Technology (BUET), East Campus, Dhaka 1000, Bangladesh. E-mail: kmshorowordi@mme.buet.ac.bd

<sup>b</sup> Pilot Plant and Process Development Centre, Bangladesh Council of Scientific and Industrial Research, Dhaka 1205, Bangladesh. E-mail: a\_nafis\_ahmed@bcsir.gov.bd

† Electronic supplementary information (ESI) available. See DOI: <https://doi.org/10.1039/d4ma01212g>



the formula  $M_{n+1}X_nT_x$  ( $n = 1-4$ ), where M denotes transition metals, X denotes carbon (C) and/or nitrogen (N), and  $T_x$  is the surface terminator group (e.g.,  $-OH$ ,  $=O$ , and  $-F$ ).<sup>8</sup> It can be produced from its precursor, MAX phases ( $M_{n+1}AX_n$ , where A belongs to A-group elements) by etching out the A layers.

MXene materials, with their layered structure, unique electrical properties, and tunable surface properties with diverse terminator groups, hold great promise for flexible electrochemical energy storage applications.<sup>9</sup> MXenes exhibit high volumetric capacitance, pseudocapacitive characteristics, and durability.<sup>10</sup> Extensive research has focused on developing MXene-based composites and heterostructures that exhibit excellent electrochemical performance. Y. Dai *et al.* developed a MXene-CoNiZn-layered double hydroxide (LDH) composite possessing a 3D honeycomb structure with an extremely high specific capacitance of  $2044.9 \text{ F g}^{-1}$  with a retention of 87.8% after 100 000 cycles.<sup>11</sup> To enhance electrochemical performance, researchers have also developed vertically aligned 3D porous nanosheets by combining two 2D materials, graphene and MXenes. These electrodes not only achieved an impressive capacitance of  $108 \text{ F g}^{-1}$  at  $1 \text{ A g}^{-1}$  scan rate but also demonstrated good cycling stability, retaining 82% of their initial capacitance over 10 000 cycles.<sup>12</sup> Additionally, MXene-transition metal chalcogenides (TMCs) (e.g.,  $\text{TiSe}_2/\text{MXene}$ , and  $\text{CoS}/\text{MXene}$ ) have been successfully synthesized to enhance the ion storage capabilities by improving the charge transfer kinetics.<sup>13,14</sup> Therefore, MXene-based composites have opened numerous opportunities for research in the field of electrochemical energy storage.

Recent studies reveal that integrating nanoparticles, such as transition metal oxides  $\text{MnO}_2$ ,  $\text{RuO}_2$ , and  $\text{TiO}_2$ , can significantly increase the electrochemical performance of MXenes by inhibiting the restacking of the latter.<sup>15,16</sup>  $\text{TiO}_2$  has gained much attention among researchers because it is one of the most stable, non-toxic, and inexpensive transition metal oxides available, particularly for supercapacitor applications.<sup>17</sup>  $\text{TiO}_2$ -MXene nanocomposites have been fabricated using various hydrothermal processes to study the synergistic effect of  $\text{TiO}_2$  and MXene phases.<sup>10,18,19</sup> J. F. Zhu *et al.* have synthesized  $\text{TiO}_2$  nanoparticle-decorated  $\text{Ti}_3\text{C}_2$  MXenes by *in situ* hydrolysis. The fabricated nanocomposite demonstrated a specific capacitance of  $143 \text{ F g}^{-1}$  at a  $5 \text{ mV s}^{-1}$  scan rate, outperforming the pristine  $\text{Ti}_3\text{C}_2$  MXene ( $93 \text{ F g}^{-1}$ ). Additionally, the nanocomposite exhibited a 92% capacitance retention up to 6000 cycles, suggesting excellent cycling stability.<sup>20</sup> However, oxidation and stacking issues during hydrofluoric acid (HF) etching are the major drawbacks of this process.<sup>21</sup> Some studies demonstrated a technique of partially oxidizing  $\text{Ti}_2\text{CT}_x$  MXene and forming a  $\text{TiO}_2$ -MXene hybrid structure by hydrogen peroxide ( $\text{H}_2\text{O}_2$ ) treatment.<sup>22,23</sup> Although the performance obtained by utilizing this technique is outstanding, it involves handling  $\text{H}_2\text{O}_2$  chemicals that spread toxicity in many mechanisms, namely corrosion, oxygen formation, and lipid peroxidation.<sup>24</sup> Another peculiar technique is to obtain  $\text{TiO}_2$ - $\text{Ti}_3\text{C}_2\text{T}_x$  MXene nanocomposites by flash oxidation in air.<sup>25,26</sup> However, this technique is quite challenging to control, particularly when powder ignition occurs, resulting in limited usage. In a similar

study by R. B. Rakhi *et al.*, the electrochemical properties of  $\text{TiO}_2$ - $\text{Ti}_2\text{CT}_x$  MXene synthesized *via* annealing in the air at 500 K for 2 hours were examined.<sup>27</sup> Moreover, the existing methodologies don't provide precise quantification of the amount of  $\text{TiO}_2$  in MXenes, hindering the investigation of an optimum composition.

In this study, we explored a new technique called the cold-sintering process (CSP) to fabricate  $\text{TiO}_2$ - $\text{Ti}_3\text{C}_2\text{T}_x$  MXene nanocomposites. The cold-sintering method exhibits excellent potential in the fabrication of nanocomposites, which employs sintering at a low temperature ( $<350 \text{ }^\circ\text{C}$ ) and low uniaxial pressure assisted by a transient liquid phase (such as water or an organic liquid).<sup>28</sup> Furthermore, the CSP eliminates the issue of MXene composites oxidizing at high temperatures during traditional sintering methods.<sup>29</sup> It can be easily used to attach  $\text{TiO}_2$  particles on the MXene surface. Consequently, it can potentially increase the number of interacting sites facilitating the surface redox reaction and intercalation of ions, enhancing its electrochemical properties. In addition, the CSP can be used to modulate the amount of  $\text{TiO}_2$  addition precisely by directly introducing the particles into the MXene structure, thereby establishing a correlation between the  $\text{TiO}_2$  amount and the electrochemical properties. Moreover, this method opens new avenues for  $\text{TiO}_2$ - $\text{Ti}_3\text{C}_2\text{T}_x$  MXene nanocomposite fabrication that surpasses the constraints of existing techniques for electrochemical storage applications.

## 2. Experimental

### 2.1. $\text{Ti}_3\text{C}_2\text{T}_x$ MXene synthesis *via* HF etching

The synthesis procedure begins with the gradual addition of 5 g of MAX Phase ( $\text{Ti}_3\text{AlC}_2$ ) powder (obtained from Forsman Scientific, with 98% purity and a particle size of 200 mesh) into 100 mL of 48 wt% hydrofluoric acid (HF) while maintaining a constant stirring speed inside a polypropylene beaker. The etching process was carried out for 5 hours under continuous stirring at room temperature. Subsequently, the sample was segregated using centrifugation (5 minutes per cycle at 5000 rpm) and washed multiple times with DI water until the pH reached approximately 6. Afterward, the sample underwent filtration, drying in an oven at  $60 \text{ }^\circ\text{C}$  for 6 hours, and was stored in a desiccator. Notably, the  $-OH$ ,  $=O$ , and  $-F$  groups act as the surface terminators ( $T_x$ ) of the 2D layers of the MXene ( $\text{Ti}_3\text{C}_2$ ). Consequently, the chemical formula of MXenes is often written as  $\text{Ti}_3\text{C}_2\text{T}_x$ .

### 2.2. Fabrication of $\text{TiO}_2$ - $\text{Ti}_3\text{C}_2\text{T}_x$ MXene nanocomposites *via* cold sintering

The cold-sintering process (CSP) was employed to fabricate  $\text{TiO}_2$ - $\text{Ti}_3\text{C}_2\text{T}_x$  MXene nanocomposites. In this technique, the raw powders are mixed with a solvent and sintered at a low temperature and pressure. Initially, the  $\text{TiO}_2$  and  $\text{Ti}_3\text{C}_2\text{T}_x$  raw powders were mixed in an agate mortar at a weight ratio of 20 : 80 and 40 : 60, respectively. A 1 : 1 volume mixture of ethanol and deionized water was used as the solvent. The solvent acts as



a transient liquid medium facilitating mass transport and particle rearrangement during the sintering process. There are two fundamental requirements for selecting an appropriate solvent–powder: samples must be soluble or dispersible in the solvent to ensure effective mixing without any agglomeration, and the solvent's boiling temperature must be below the sintering temperature for complete evaporation promoting rearrangement of particles. Therefore, choosing the right solvent is essential. While the CSP of MXene-based composites is often carried out with a single solvent, mostly deionized water, the hydrophobic nature of  $\text{TiO}_2$  and good dispersibility in ethanol prompted the inclusion of ethanol.<sup>30</sup> Furthermore, deionized water and ethanol both have low boiling points, which is beneficial for the cold sintering process. Subsequently, the resulting sample was inserted into a stainless-steel die (12 mm diameter) and placed in a hot press machine. The sample was sintered using 150 °C temperature and 150 MPa pressure for 45 minutes. Finally, the sintered pellets were removed carefully. A schematic of the cold sintering process is given in Fig. 1.

### 2.3. Fabrication of working electrodes

Initially, the pellet samples were ground into powder. Subsequently, the powder was mixed with carbon black and 4% (w/v) PVA binder at a weight ratio 80 : 15 : 5. The powder mixture was transformed into a slurry by adding ethanol. The working electrode was formed by coating the slurry on a conductive graphite rod (average diameter 8 mm). After drying the electrode for 24 hours, Teflon tape was wrapped around it, exposing a surface with a square-shaped area of approximately 16 mm<sup>2</sup>. Following this process, working electrodes were fabricated for the as-synthesized  $\text{Ti}_3\text{C}_2\text{T}_x$  MXene powder,  $\text{TiO}_2$  powder, (20 wt%)  $\text{TiO}_2/\text{MXene}$ , and (40 wt%)  $\text{TiO}_2/\text{MXene}$  nanocomposites. A schematic illustration of the working electrode preparation steps can be found in the ESI† (Fig. S1).

### 2.4. Characterization

X-ray diffraction (XRD) spectra were obtained using an EMPYR-EAN multi-purpose diffractometer with  $\text{Cu-K}\alpha$  radiation of wavelength  $\lambda = 1.54060 \text{ \AA}$  at 40 mA and 45 kV. Field-emission scanning microscopy (FESEM) was performed using a JOEL JSM-7600F for the as-synthesized MXene sample and TESCAN

VEGA COMPACT for the nanocomposite samples. X-ray photoelectron spectroscopy (XPS) analysis was conducted using  $\text{Al K}\alpha$  radiation on the as-prepared MXene sample. Electrochemical characterization, *viz.* cyclic voltammetry and electrochemical impedance spectroscopy (EIS) of the samples, was performed utilizing a Gamry 3000AE potentiostat utilizing a three-electrode setup. It comprises a fabricated working electrode, a platinum wire as the counter electrode, a saturated calomel electrode (SCE) as the reference electrode and 1 M KOH solution as the electrolyte. Cyclic voltammograms were recorded at different scan rates, including 10, 20, 50, and 100  $\text{mV s}^{-1}$ , at a potential window of  $-1 \text{ V}$  to  $0.5 \text{ V}$  (*vs.* SCE). Electrochemical impedance spectroscopy (EIS) was performed at frequencies ranging from 100 kHz to 0.01 Hz. All electrochemical tests were performed at room temperature.

## 3. Results and discussion

### 3.1. Structural, morphological, and chemical bond analysis of $\text{Ti}_3\text{C}_2\text{T}_x$ MXene

The XRD patterns of the initial raw  $\text{Ti}_3\text{AlC}_2$  MAX-phase (ICSD:153266) powder and the synthesized MXene obtained through HF treatment are shown in Fig. 2(a). A low-intensity peak of  $\text{TiC}$  (ICSD:159871) was observed in the XRD pattern for the MAX-phase, which is most likely to originate from the precursors used as a source of carbon to synthesize the MAX-phase.<sup>31–33</sup> The XRD pattern of MXene is in agreement with that in the published literature.<sup>34,35</sup> As shown in Fig. 2(a), the characteristic peak of the MAX-phase at  $2\theta = 39^\circ$  has completely disappeared, indicating the successful etching of the Al layer.<sup>36,37</sup> On the other hand, the (002) and (004) peaks have shifted to a lower angle, suggesting an increase in interlayer spacing due to the addition of surface terminator groups ( $-\text{F}$ ,  $=\text{O}$  and/or  $-\text{OH}$ ). Based on the (004) plane, the crystallite size, dislocation density ( $\delta$ ), micro-strain ( $\epsilon$ ), and lattice constants were calculated using eqn (S1)–(S4) listed in the ESI.† As indicated in Table 1, the etching of the Al layer led to a substantial reduction in the crystallite size. The crystallographic changes are further discussed in Section 3.2.

The XRD pattern of  $\text{TiO}_2$  powder, shown in Fig. 2(b), reveals that most of the peaks correspond to the Rutile  $\text{TiO}_2$  (ICSD:168138) with the  $P4_2/mnm$  space group. However, a low-intensity peak at

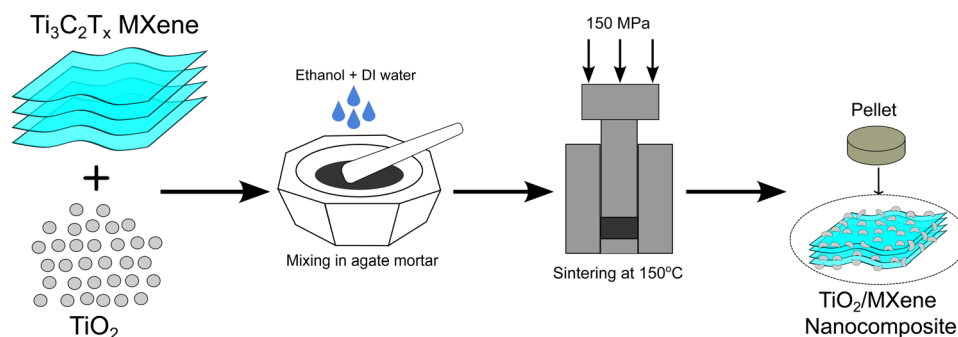


Fig. 1 Schematic illustration showing the cold sintering process (CSP) to fabricate  $\text{TiO}_2/\text{MXene}$  nanocomposites.



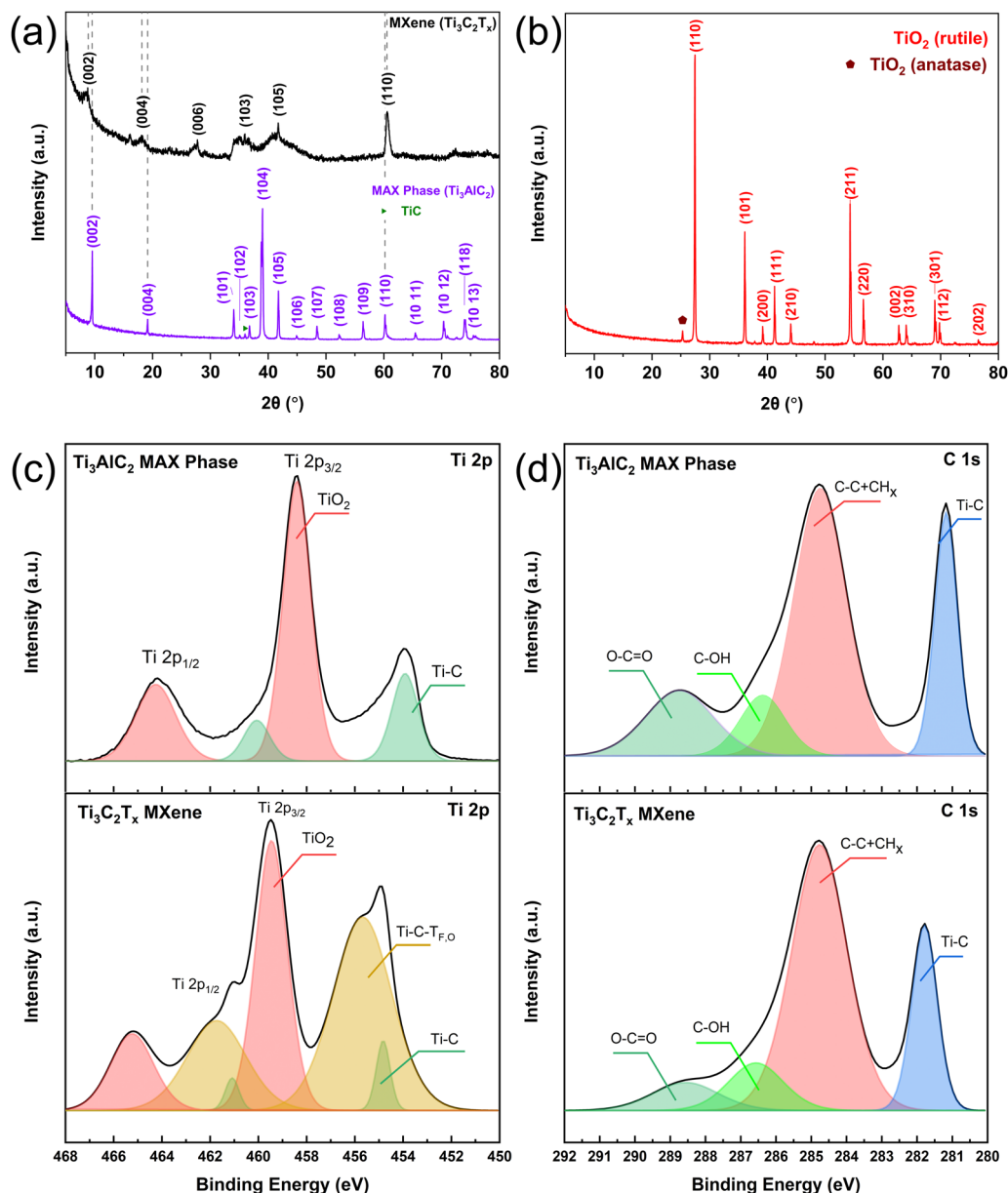


Fig. 2 XRD patterns of the (a) MAX phase and MXene, (b) TiO<sub>2</sub>; high-resolution XPS spectra of (c) Ti 2p and (d) C 1s in the Ti<sub>3</sub>AlC<sub>2</sub> MAX phase and Ti<sub>3</sub>C<sub>2</sub>T<sub>x</sub> MXene samples.

Table 1 Diffraction parameters from XRD for the MAX-phase, MXene, and cold-sintered TiO<sub>2</sub>/MXene nanocomposites for the (110) plane. Lattice constants are calculated using the (004) and (110) planes

Sample	$d$ -spacing (Å) (004)	$d$ -spacing (Å) (110)	Crystallite size (L) (nm)	Dislocation density ( $\delta \times 10^{-3}$ ) (nm <sup>-1</sup> )	Micro-strain ( $\epsilon \times 10^{-3}$ )	Lattice parameter	
						$a$ (Å)	$c$ (Å)
Ti <sub>3</sub> AlC <sub>2</sub> MAX-phase	4.63	1.54	93.74	0.11	0.77	3.07	18.52
Ti <sub>3</sub> C <sub>2</sub> T <sub>x</sub> MXene powder	4.88	1.53	18.77	2.84	3.83	3.06	19.52
100 wt% MXene pellet	4.90	1.531	31.27	1.02	2.30	3.06	19.60
(20 wt%) TiO <sub>2</sub> /MXene pellet	4.86	1.526	15.66	4.08	4.58	3.06	19.46
(40 wt%) TiO <sub>2</sub> /MXene pellet	4.92	1.525	15.38	4.23	4.66	3.05	19.68

$2\theta \approx 25.3^\circ$  was observed that corresponds to the (101) plane of anatase TiO<sub>2</sub> (ICSD:121634) with the  $I4_1/amd$  space group.

This suggests that the TiO<sub>2</sub> powder consisted predominantly of the rutile phase along with a trace amount of the anatase impurity phase.



**Table 2** Binding energies for Ti 2p and C 1s from the Ti<sub>3</sub>AlC<sub>2</sub> MAX phase and Ti<sub>3</sub>C<sub>2</sub>T<sub>x</sub> MXene XPS spectra

Ti 2p				
Compound	Component	2p <sub>3/2</sub> (eV)	2p <sub>1/2</sub> (eV)	ΔBE (eV)
Ti <sub>3</sub> AlC <sub>2</sub> MAX phase	Ti–C	453.88	460.08	6.20
	TiO <sub>2</sub>	458.38	464.28	5.90
Ti <sub>3</sub> C <sub>2</sub> T <sub>x</sub> MXene	Ti–C	454.78	461.08	6.30
	Ti–C–T <sub>F,O</sub>	455.68	461.78	6.10
	TiO <sub>2</sub>	459.48	465.28	5.80

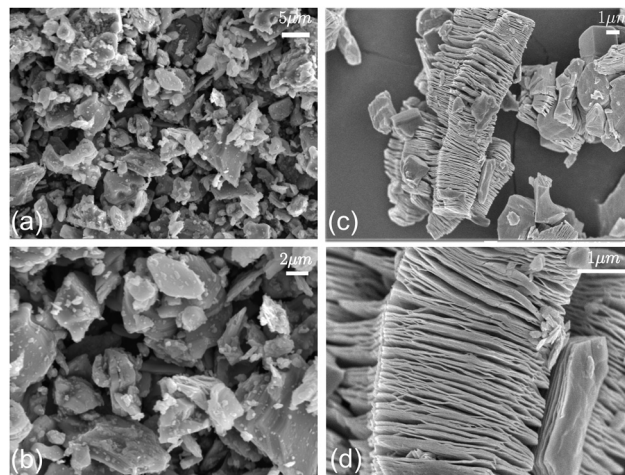
  

C 1s		
Compound	Component	1s (eV)
Ti <sub>3</sub> AlC <sub>2</sub> MAX phase	Ti–C	281.18
	C–C + CH <sub>x</sub>	284.78
	C–OH	286.38
	O–C=O	288.78
Ti <sub>3</sub> C <sub>2</sub> T <sub>x</sub> MXene	Ti–C	281.78
	C–C + CH <sub>x</sub>	284.78
	C–OH	286.58
	O–C=O	288.58

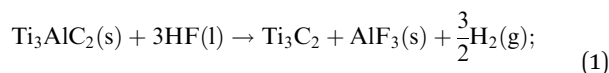
X-ray photoelectron spectroscopy was performed on the Ti<sub>3</sub>AlC<sub>2</sub> MAX phase and Ti<sub>3</sub>C<sub>2</sub>T<sub>x</sub> MXene was synthesized to investigate the changes induced by the HF etching process. Fig. 2 presents the XPS spectra of the Ti 2p and C 1s regions of the samples, while the corresponding peak binding energies are summarized in Table 2.

Fig. 2(c) shows the Ti 2p XPS spectra of the Ti<sub>3</sub>AlC<sub>2</sub> MAX phase and Ti<sub>3</sub>C<sub>2</sub>T<sub>x</sub> MXene, deconvoluted into 2p<sub>3/2</sub> and 2p<sub>1/2</sub> spin-orbit split components. In the MAX phase, the 2p<sub>3/2</sub> peaks corresponding to Ti–C and TiO<sub>2</sub> were observed at binding energies of 453.88 and 458.38 eV, respectively. In contrast, the MXene spectra revealed a new bond corresponding to 2p<sub>3/2</sub> Ti–C–T<sub>F,O</sub> at a binding energy of 455.68 eV, indicating the presence of surface terminator groups.<sup>38</sup> Furthermore, a slight shifting in the binding energies of Ti–C and TiO<sub>2</sub> suggests modifications in the electron density due to the addition of the surface terminator group (–F, =O or –OH).<sup>20</sup> This can be further confirmed by the slight positive shift in C 1s binding energies for Ti–C, C–OH, and O–C=O, as indicated by Fig. 2(d) and Table 2. Additionally, the XPS survey plots shown in Fig. S2 (ESI<sup>†</sup>) revealed that the peaks for Al exhibit a significant loss of intensity in the synthesized MXene indicating successful etching of the Al-layer from the MAX phase.

The morphological and compositional analysis of the as-synthesized Ti<sub>3</sub>C<sub>2</sub>T<sub>x</sub> MXene was done utilizing SEM and EDS. As shown in the SEM images in Fig. 3, the synthesized Ti<sub>3</sub>C<sub>2</sub>T<sub>x</sub> MXene exhibits a flake-like structure composed of multiple 2D layers. This multilayer structure is attributed to the successful etching of the Al layer.<sup>39,40</sup> The EDS analysis on two distinct points suggests the presence of Ti, C, O, F, and Al with a descending atomic percentage, respectively (Fig. S3 and Table S1, ESI<sup>†</sup>). While the presence of O and F indicates the terminator group (T<sub>x</sub>) of the MXene, the presence of Al suggests the formation of AlF<sub>3</sub> impurities during the etching process, as indicated by the chemical eqn (1).<sup>41–43</sup> These impurities appear as small ball-like particles on the surface of the flakes. It is

**Fig. 3** SEM images of the (a) and (b) MAX phase (Ti<sub>3</sub>AlC<sub>2</sub>) and (c) and (d) synthesized MXene (Ti<sub>3</sub>C<sub>2</sub>T<sub>x</sub>) at (a), (c) 5000×, (b) 10 000×, and (d) 20 000× magnifications.

imperative to minimize such impurities as they tend to adversely affect MXene crystallinity and produce inconsistency in the surface termination groups (T<sub>x</sub>).<sup>44</sup> This poses a negative influence on the faradaic reactions during electrochemical processes resulting in reduced performance. After the synthesis reaction, the powder sample is washed multiple times with DI-water to segregate the impurities minimizing the amount of AlF<sub>3</sub> on the MXene surface.



$$\Delta H_{25^\circ\text{C}} = -2186 \pm 34.01 \text{ kJ mol}^{-1}$$

### 3.2. Structural and morphological analysis of TiO<sub>2</sub>–Ti<sub>3</sub>C<sub>2</sub>T<sub>x</sub> MXene nanocomposites

The XRD characterization was conducted on nanocomposite pellets to investigate the crystallographic changes associated with adding TiO<sub>2</sub>. Additionally, a 100 wt% MXene pellet was also analyzed to observe the changes resulting exclusively from the temperature (150 °C) and pressure (150 MPa) applied during the cold sintering process. The XRD patterns for the samples are shown in Fig. 4(a). Several low-intensity peaks corresponding to TiC (ICSD:181681) and TiOF<sub>2</sub> (ICSD:38132) were observed in both the 100 wt% MXene pellet and (20 wt%) TiO<sub>2</sub>/MXene pellet. However, these peaks were absent for the (40 wt%) TiO<sub>2</sub>/MXene pellet, suggesting that a more significant amount of TiO<sub>2</sub> reduces the tendency of external phase formation. Furthermore, specific peaks of the MXene disappear entirely with the addition of TiO<sub>2</sub>. For example, peaks at 2θ ≈ 8.6°, 36.7°, and 41.63° correspond to (002), (103), and (105), respectively. In contrast, the peaks from the (004), (006), and (110) planes of MXenes didn't disappear entirely. Rather, their intensities were substantially reduced with the increasing amount of TiO<sub>2</sub>. Notably, the attenuation of the intensity of the (110) peak indicates significant rearrangements of atoms away from the preferred (110) plane orientation.



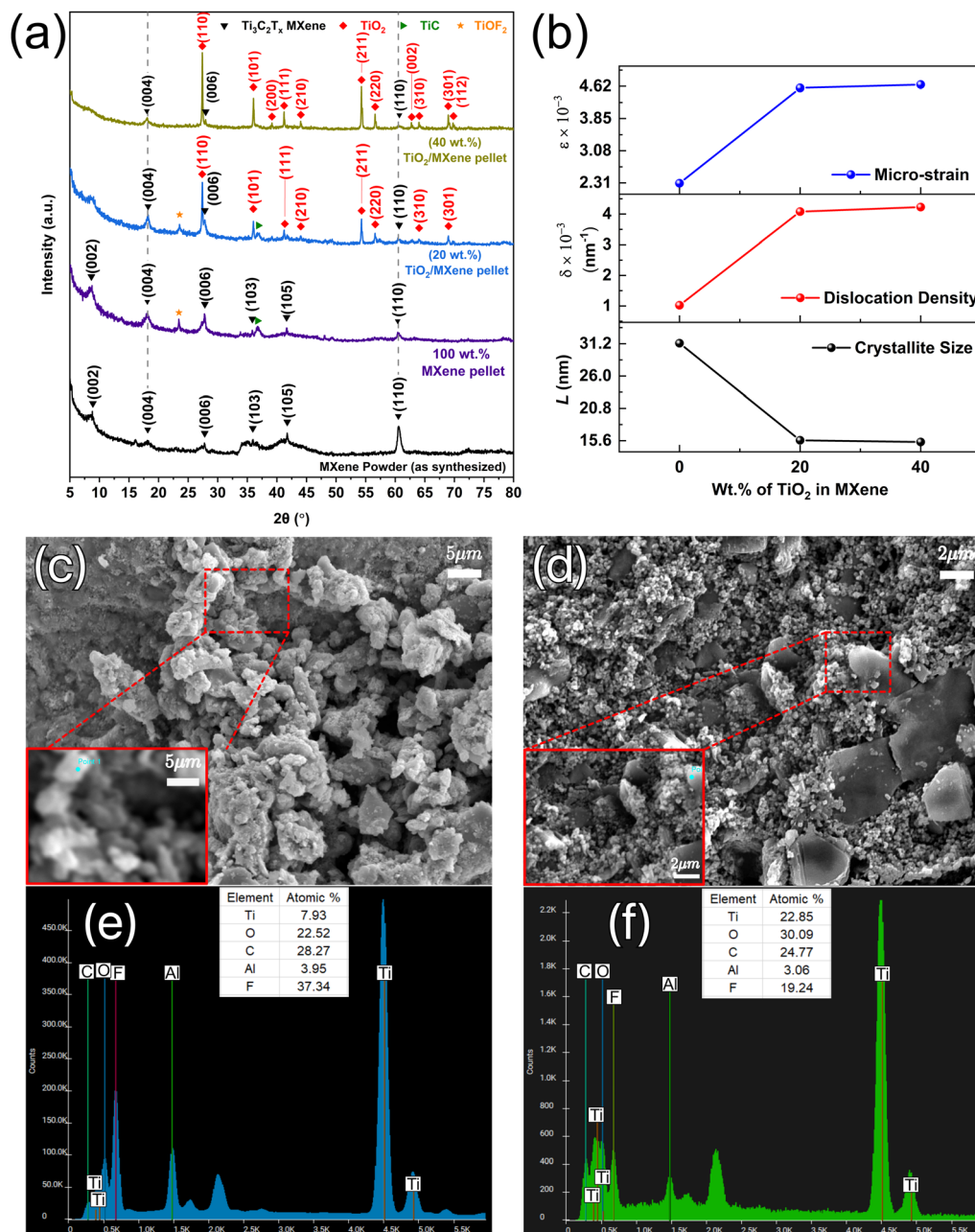


Fig. 4 (a) XRD patterns for as-synthesized MXene powder and cold-sintered nanocomposite pellets, (b) the variation of the crystallite size ( $L$ ), dislocation density ( $\delta$ ), and micro-strain ( $\epsilon$ ) as a function of the weight percentage of TiO<sub>2</sub> in the MXene cold-sintered at 150 °C temperature and 150 MPa pressure, and the SEM-EDS images of the (c) and (e) (20 wt%) TiO<sub>2</sub>/MXene and (d) and (f) (40 wt%) TiO<sub>2</sub>/MXene nanocomposites.

As depicted in Table 1, the initial increase in the  $d$ -spacing and crystallite size, along with the decrease in the dislocation density and micro-strain, is exclusively due to the applied temperature (150 °C) and pressure (150 MPa) during the cold sintering process. As indicated in Fig. 4(b), the crystallite size decreases with the addition of 20 wt% TiO<sub>2</sub> compared to no addition (100 wt% MXene pellets). In contrast, an increase is observed for both the dislocation density and micro-strain. Furthermore, all these values remain stable with the further addition of TiO<sub>2</sub> (40 wt%) to MXenes. This stability is attributed to the fact that the applied temperature (150 °C) and pressure

(150 MPa) during the cold sintering process were the same for all samples. Overall, the amount of TiO<sub>2</sub> and cold sintering parameters are the key factors influencing the crystallographic diffraction patterns of the nanocomposite samples.

Several previous studies developed TiO<sub>2</sub>-MXene nanocomposites *via* the chemical formation of TiO<sub>2</sub> on the MXene surface using methods such as flash oxidation, H<sub>2</sub>O<sub>2</sub>-assisted oxidation, thermal annealing in air, and other hydrothermal reactions.<sup>20,22,25,27</sup> The XRD results of these studies indicate that there is an increase in crystallinity after TiO<sub>2</sub>-MXene composite formation, judging by the peak sharpness and



signal-to-noise ratio. In the CSP method, a similar increase of crystallinity can be observed, as indicated by the reduced noise and increased peak sharpness for the TiO<sub>2</sub>-MXene nanocomposites shown in Fig. 4(a). In addition, the crystallite size, dislocation density, and micro-strain remained almost constant after forming composites using the CSP, as indicated in Fig. 4(b). Therefore, the key advantage of the CSP over traditional methods is to offer the ability to control the size and distribution of crystallites using only two parameters, namely temperature and pressure.

Interestingly, all of the previous studies reported deposition of nanocrystalline anatase-TiO<sub>2</sub> on the MXene. In contrast, rutile-TiO<sub>2</sub> particles were successfully incorporated onto the MXene surface using the CSP. While both phases exhibit a high degree of crystallinity, the rutile-TiO<sub>2</sub> phase offers greater stability.<sup>45</sup> Additionally, impurity phases such as TiC and TiOF<sub>2</sub> were also detected at a low composition, as can be seen in Fig. 4(a). Despite being impurities, recent studies suggest that the formation of TiC and TiOF<sub>2</sub> can actually enhance the electrochemical performance of MXenes for supercapacitor and lithium-ion battery applications.<sup>46,47</sup> Therefore, CSP presents a novel way to customize and improve the electrochemical properties of MXene-based nanocomposites.

The morphological and chemical composition of the fabricated TiO<sub>2</sub>-MXene nanocomposites were investigated utilizing SEM and EDS. As shown in the SEM images in Fig. 4(c) and (d), the nanoparticles of TiO<sub>2</sub> adorn the surface of MXenes in a random pattern, forming a coagulated structure. The cold-sintered (20 wt%) TiO<sub>2</sub>/MXene and (40 wt%) TiO<sub>2</sub>/MXene nanocomposites have relatively compact structures. It can also be represented using the relative density calculations shown in Section 3.3. The adsorption of TiO<sub>2</sub> particles on the MXene sheets increases the surface area and has a roughening effect. Consequently, this morphology would contribute to the increased number of interaction sites for the faradaic redox process during electrochemical cycling, which substantially influences the capacitive response of the samples.<sup>27,48</sup> The distribution of Ti, Al, C, O, and F in the cold-sintered TiO<sub>2</sub>-MXene nanocomposite samples are shown in the EDS images in Fig. 4(e) and (f). While the atomic percentage for O (22.52%) is lower than that for F (37.34%) in the (20 wt%) TiO<sub>2</sub>/MXene sample, the atomic percentage for O (30.09%) exceeded that for F (19.24%) in the (40 wt%) TiO<sub>2</sub>/MXene sample. Furthermore, the atomic percentage of Ti increased from 7.93% to 22.85% with TiO<sub>2</sub> particle addition, contributing to the alteration of the MXene surface.

### 3.3. Relative density measurements

Relative density can be defined as the proportion of the theoretical density achieved after sintering. It is used to quantify the quality of a cold-sintered composite. The density of the samples was determined using the conventional weight-to-volume ratio of the sintered pellets. On the other hand, the theoretical density ( $\rho_{th}$ ) and relative density ( $\rho_r$ ) of the composite were calculated using the formula shown in eqn (2) and (3).

Table 3 Mean and standard deviations of the sintered and relative densities (%) for the cold-sintered samples

Sample	Sintered density (g cc <sup>-1</sup> )	Relative density (%)
100 wt% MXene	3.24 ± 0.04	88.57 ± 1.17
(20 wt%) TiO <sub>2</sub> /MXene	3.38 ± 0.08	88.67 ± 2.04
(40 wt%) TiO <sub>2</sub> /MXene	3.49 ± 0.09	89.00 ± 2.42

$$\text{Theoretical density: } \rho_{th} = (f \times \rho_{TiO_2}) + (1 - f) \times \rho_{MXene} \quad (2)$$

$$\text{Relative density: } \rho_r = \left( \frac{\rho}{\rho_{th}} \right) \times 100\% \quad (3)$$

Here,  $\rho$  = the density of the sintered pellet and  $\rho_{th}$  = the theoretical density of the composite,  $f$  = weight fraction of reinforcement (TiO<sub>2</sub>),  $\rho_{TiO_2}$  = density of TiO<sub>2</sub> (4.249 g cc<sup>-1</sup>),<sup>49</sup> and  $\rho_{MXene}$  = density of the Ti<sub>3</sub>C<sub>2</sub>T<sub>x</sub> MXene (3.7 g cc<sup>-1</sup>).<sup>50</sup> A summary of the relative density measurements is shown in Table 3. Notably, more than 85% of the relative density indicated good densification.

### 3.4. Electrochemical performance analysis

The electrochemical performance of the fabricated nanocomposites is analyzed *via* cyclic voltammetry (CV), electrochemical impedance spectroscopy (EIS), and galvanostatic charging-discharging (GCD) tests using a three-electrode system. The cyclic voltammetry (CV) test provides valuable insights into the charge transfer rate at the electrolyte and electrode interface. The cyclic voltammograms of the pure Ti<sub>3</sub>C<sub>2</sub>T<sub>x</sub> MXene, pure TiO<sub>2</sub>, and TiO<sub>2</sub>/MXene nanocomposite samples are shown in Fig. 5(a)-(d). The curves exhibit a quasi-rectangular shape with a symmetric current response during both anodic and cathodic potential scans, suggesting pseudocapacitive behavior.<sup>51</sup> This type of response is due to the reversible faradaic mechanism of pseudocapacitors involving the surface redox reaction attributed to the change of the oxidation state of Ti. Notably, the current response is higher as the scan rate increases, resulting in a larger loop area. This phenomenon is due to the change in resistance associated with the electrolyte ion diffusion layer with varying scan rates. At lower scan rates, the electrolyte ion diffusion layer thickness formed at the electrode surface is larger, leading to a high charge transfer resistance and making the loop of area small. However, the diffusion layer thickness depletion lowers the charge-transfer resistance as the scan rate increases. As a result, a higher amount of charge transfer increases the CV curve loop area. However, a higher scan rate substantially reduces the rate of inner-surface adsorption of ions, thus lowering the specific capacitance value.<sup>52</sup>

Fig. 5(e) illustrates the cyclic voltammetry curve at a fixed scan rate of 10 mV s<sup>-1</sup>. TiO<sub>2</sub> exhibits the lowest electrochemical activity, as indicated by the smallest loop area. However, the loop area increases when TiO<sub>2</sub> is integrated with MXenes to form nanocomposites, suggesting enhanced electrochemical response. This implies that adding TiO<sub>2</sub> improves the pseudocapacitive electrochemical performance of the MXene. The specific



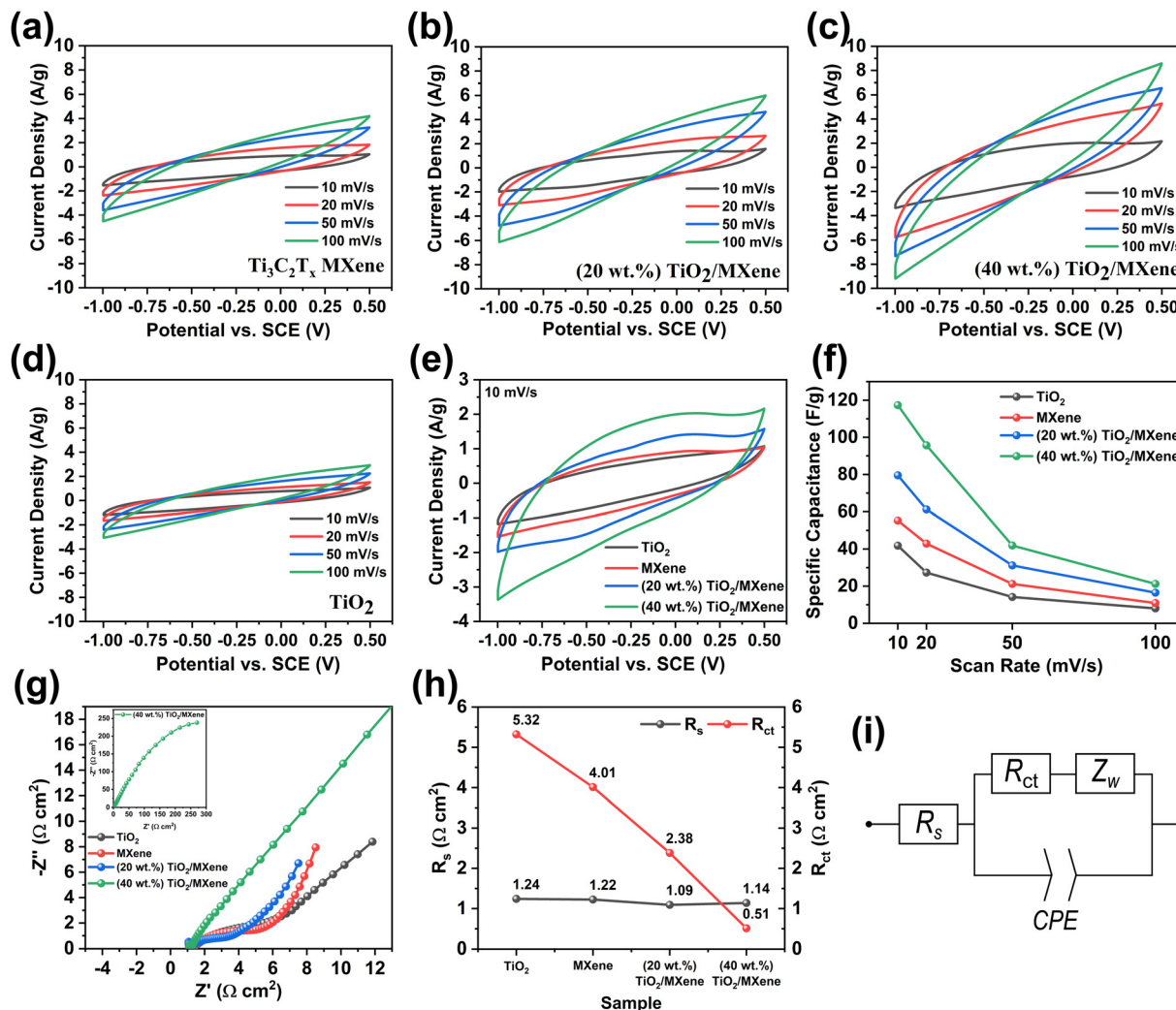


Fig. 5 Cyclic voltammograms of the (a)  $\text{Ti}_3\text{C}_2\text{T}_x$  MXene, (b) (20 wt%)  $\text{TiO}_2/\text{MXene}$ , (c) (40 wt%)  $\text{TiO}_2/\text{MXene}$  (d) pure  $\text{TiO}_2$  electrodes at various scan rates, and (e) all electrode samples at a  $10 \text{ mV s}^{-1}$  scan rate, (f) specific capacitance values as a function of scan rate; (g) Nyquist plots of  $\text{TiO}_2$ , MXene, (20 wt%)  $\text{TiO}_2/\text{MXene}$ , and (40 wt%)  $\text{TiO}_2/\text{MXene}$  electrodes (inset: Nyquist plot for (40 wt%)  $\text{TiO}_2/\text{MXene}$  including the low-frequency region); (h) equivalent series resistance or solution resistance ( $R_s$ ) and charge transfer resistance ( $R_{ct}$ ) values for  $\text{TiO}_2$ , MXene,  $\text{TiO}_2/\text{MXene}$ ; (i) (equivalent circuit for the constant phase element (CPE) with diffusion).

capacitance ( $C_s$ ) values were calculated using eqn (4).

$$C_s = \frac{\int I(V)dV}{ms\Delta V} \quad (4)$$

Here,  $\int I(V)dV =$  integral area of the CV curve ( $\text{C s}^{-1} \text{V}$ ),  $m =$  active mass of the working material (g),  $s =$  scan rate ( $\text{V s}^{-1}$ ), and  $\Delta V =$  potential window (V).

As indicated by Table 4 and Fig. 5(f), the specific capacitance for the  $\text{TiO}_2/\text{MXene}$  nanocomposites samples was consistently greater compared to that for pristine  $\text{TiO}_2$  and MXene for all the scan rates. However, these values decline exponentially with the increasing scan rate. This trend is attributed to the reduced number of effectively adsorbed ions at the inner surface of the electrodes.<sup>52</sup> The highest specific capacitance value,  $117.34 \text{ F g}^{-1}$ , was achieved for (40 wt%)  $\text{TiO}_2/\text{MXene}$  nanocomposites at a scan rate of  $10 \text{ mV s}^{-1}$ . In contrast, pure  $\text{TiO}_2$  exhibits the lowest specific capacitance of  $41.80 \text{ F g}^{-1}$  (at  $10 \text{ mV s}^{-1}$ ) due to its poor

capacitive nature, which can be observed in the CV curves as well (Fig. 5(d)).

According to the comparison shown in Table 5, our highest achieved capacitance,  $117.34 \text{ F g}^{-1}$ , is quite reasonable compared to a  $\text{TiO}_2$  (anatase)-MXene nanocomposite synthesized using the *in situ* hydrolysis process, which achieved a specific capacitance of  $143 \text{ F g}^{-1}$  at a  $5 \text{ mV s}^{-1}$  scan rate.<sup>20</sup> The offset can be attributed to the use of different scan rates. As explained earlier, at higher scan rates, the specific capacitance is achieved due to the lower diffusion of ions. The composite samples synthesized using the post-etching annealing air method proposed by Rakhi *et al.* exhibited a low specific capacitance ( $\sim 5 \text{ F g}^{-1}$  at  $5 \text{ mV s}^{-1}$ ), indicating poor performance.<sup>27</sup> Furthermore, the capacitance retention performance using the CSP method is comparatively greater than that of existing fabrication methods. Additional experimental parameters and the electrochemical cyclic performance are summarized in



**Table 4** The specific capacitance values for prepared electrodes were measured at a potential window from  $-1$  to  $0.5$  V in  $1$  M KOH solution

	Scan rate ( $\text{mV s}^{-1}$ )	Specific capacitance ( $C_s$ ) ( $\text{F g}^{-1}$ )			
		MXene	(20 wt%) TiO <sub>2</sub> /MXene	(40 wt%) TiO <sub>2</sub> /MXene	TiO <sub>2</sub>
Cyclic voltammetry	10	55.29	79.52	117.34	41.80
	20	42.90	61.20	95.67	27.30
	50	21.24	31.18	41.93	14.17
	100	10.93	16.51	21.25	8.03

	Current density ( $\text{A g}^{-1}$ )	Specific capacitance ( $C_s$ ) ( $\text{F g}^{-1}$ )			
		MXene	(20 wt%) TiO <sub>2</sub> /MXene	(40 wt%) TiO <sub>2</sub> /MXene	TiO <sub>2</sub>
Galvanostatic charge-discharge	0.5	42.92	26.84	45.32	17.81
	1.0	34.84	14.69	14.21	5.79
	1.5	16.14	20.73	12.45	1.16
	2.0	11.30	3.21	0.65	1.35

Table 5. These results suggest that cold sintering can be a viable process for fabricating TiO<sub>2</sub>-MXene nanocomposites capable of producing competitive results, with only a 19% offset, compared to other conventional methods.

The EIS technique investigates the charge transfer trends and the overall resistive properties of the components, including the electrolytes and electrode material, in an electrochemical system. A typical electrochemical system is composed of various complex components such as, charge transfer, ion-diffusion, double-layer capacitance, solution resistance, *etc.* Each of these components contribute to the overall impedance in the form of electrical elements (*e.g.*, resistors, capacitors, inductors, constant phase element (CPE), Warburg element, *etc.*) plotted in the Nyquist plot. These components are mathematically modeled *via* an equivalent circuit fitting the experimental Nyquist plot.<sup>53</sup> A Nyquist plot represents the imaginary impedance,  $Z''$  (reactance), on the  $y$ -axis against the real impedance and  $Z$  (resistance), on the  $x$ -axis. It is divided into several frequency regions, including a linear line at the low-frequency region denoting capacitive properties, followed by an intermediate-frequency region (Warburg zone) relating the interaction between the electrode porosity and electrolyte ions, and a semi-circular shaped high-frequency region infers the charge transfer resistance ( $R_{ct}$ ). The value of  $R_{ct}$  is calculated by measuring the diameter of the semi-circle at the high-frequency region. Additionally, the point EIS spectra cut the real axis, or the  $x$ -axis represents the solution resistance ( $R_s$ ), also denoted as the equivalent series resistance (ESR).

The Nyquist plots for TiO<sub>2</sub>, MXene, and TiO<sub>2</sub>/MXene nanocomposites are shown in Fig. 5(g). The semi-circular region in composites is substantially smaller compared to pristine TiO<sub>2</sub> and MXene, which implies that the charge transfer resistance ( $R_{ct}$ ) has decreased. It can be further quantified by the equivalent circuit modeling with the “CPE with diffusion” circuit shown in Fig. 5(i). The reason for utilizing a constant phase element (CPE) instead of a capacitor is the non-ideal nature of the electrochemical system. Ideally, the phase angle difference between the voltage and current is  $-90^\circ$  for a capacitor. However, in many cases especially for pseudocapacitive materials, the capacitive behavior is non-ideal due to the presence of structural or kinetic heterogeneities in the electrode stemming from different sources such as, surface roughness, microscopic porosity, adsorption of ions or molecules, non-uniform current distribution, *etc.*<sup>54,55</sup> The constant phase element is mathematically modeled using eqn (5), where  $Q$  = CPE constant also known as pseudocapacitance,  $j$  = imaginary unit,  $\omega$  = angular frequency,  $n$  = CPE exponent (usually ranges from 0.8 to 1.0 for the capacitive system). Notably,  $n = 1.0$  represents an ideal capacitor.

$$Z_{\text{CPE}} = \frac{1}{Q(j\omega)^n} \quad (5)$$

The decreasing trend of charge transfer resistance is shown in Fig. 5(h), indicating that the TiO<sub>2</sub>/MXene composite structure provides more active sites for the reaction and significantly improves the charge transfer. The impedance tests were conducted in  $1$  M KOH solution for all samples. Consequently, the solution resistance ( $R_s$ ) or the equivalent series resistance (ESR) should be the same for all samples. Besides, since  $1$  M KOH was utilized as the electrolyte for all the samples, the  $R_s$  value remains almost constant between  $1$  and  $1.25 \Omega \text{ cm}^2$ , as indicated in Fig. 5(h).

The GCD test is one of the most essential techniques for studying the electrochemical behavior of supercapacitor materials. The same potential range as cyclic voltammetry ( $-1$  to  $0.5$  V) was used to perform GCD tests at four distinct current densities as illustrated in Fig. 6(a)-(d). This is evident from the non-linear and asymmetric nature of the curves, which indicate pseudocapacitive behavior. The specific capacitance ( $C_s$ ) shown in Table 4, is calculated utilizing eqn (6):

$$C_s = \frac{2I_m}{(\Delta V)^2} \times \int V dt \quad (6)$$

**Table 5** Electrochemical performance comparison with the existing TiO<sub>2</sub>-MXene composition fabricated using different methodologies

Electrode material	Fabrication method	Electrolyte	Potential window	Specific capacitance	Capacitance retention/ number of cycles	Ref.
TiO <sub>2</sub> -Ti <sub>3</sub> C <sub>2</sub> T <sub>x</sub>	Cold sintering	1 M KOH	$-1.0$ to $0.5$ V ( <i>vs.</i> SCE)	$117.34 \text{ F g}^{-1}$ at $10 \text{ mV s}^{-1}$	346%/1000	This Work
TiO <sub>2</sub> -Ti <sub>3</sub> C <sub>2</sub> T <sub>x</sub>	<i>In situ</i> hydrolysis	6 M KOH	$-1.0$ to $-0.35$ ( <i>vs.</i> Ag/AgCl)	$143 \text{ F g}^{-1}$ at $5 \text{ mV s}^{-1}$	96%/3000	20
TiO <sub>2</sub> -Ti <sub>2</sub> CT <sub>x</sub>	Annealing in air at $500$ K	30 wt% KOH	$0.0$ - $0.7$ V	$\sim 5 \text{ F g}^{-1}$ at $5 \text{ mV s}^{-1}$	86%/6000	27



Here,  $I_m$  = current density ( $A\ g^{-1}$ ),  $\Delta V$  = potential window, and  $\int V dt$  = integral area under the GCD curve.

Furthermore, increasing current density yields a lower specific capacitance value due to the limited faradaic redox reaction at the electrode surface. At lower current densities, the probability of ion adsorption and intercalation is higher, which results in a higher capacitance value. By increasing the current density value, electrolyte ions remain on the outer surface of the electrode, reducing the probability of adsorption or

intercalation.<sup>56</sup> GCD tests were performed for 1000 cycles at a constant current density of  $1.5\ A\ g^{-1}$  to investigate the fabricated electrodes' cycling stability. Fig. 6(f)–(i) depicts the capacitance retention and the GCD curves for the first and last two cycles. All the samples demonstrated a significant increase in specific capacitance except pure  $TiO_2$ . The GCD data showed a decreasing trend with increasing current density. However, the  $TiO_2$  sample exhibited anomalous behavior, showing  $1.35\ F\ g^{-1}$  specific capacitance at a  $2\ A\ g^{-1}$  current density, which is

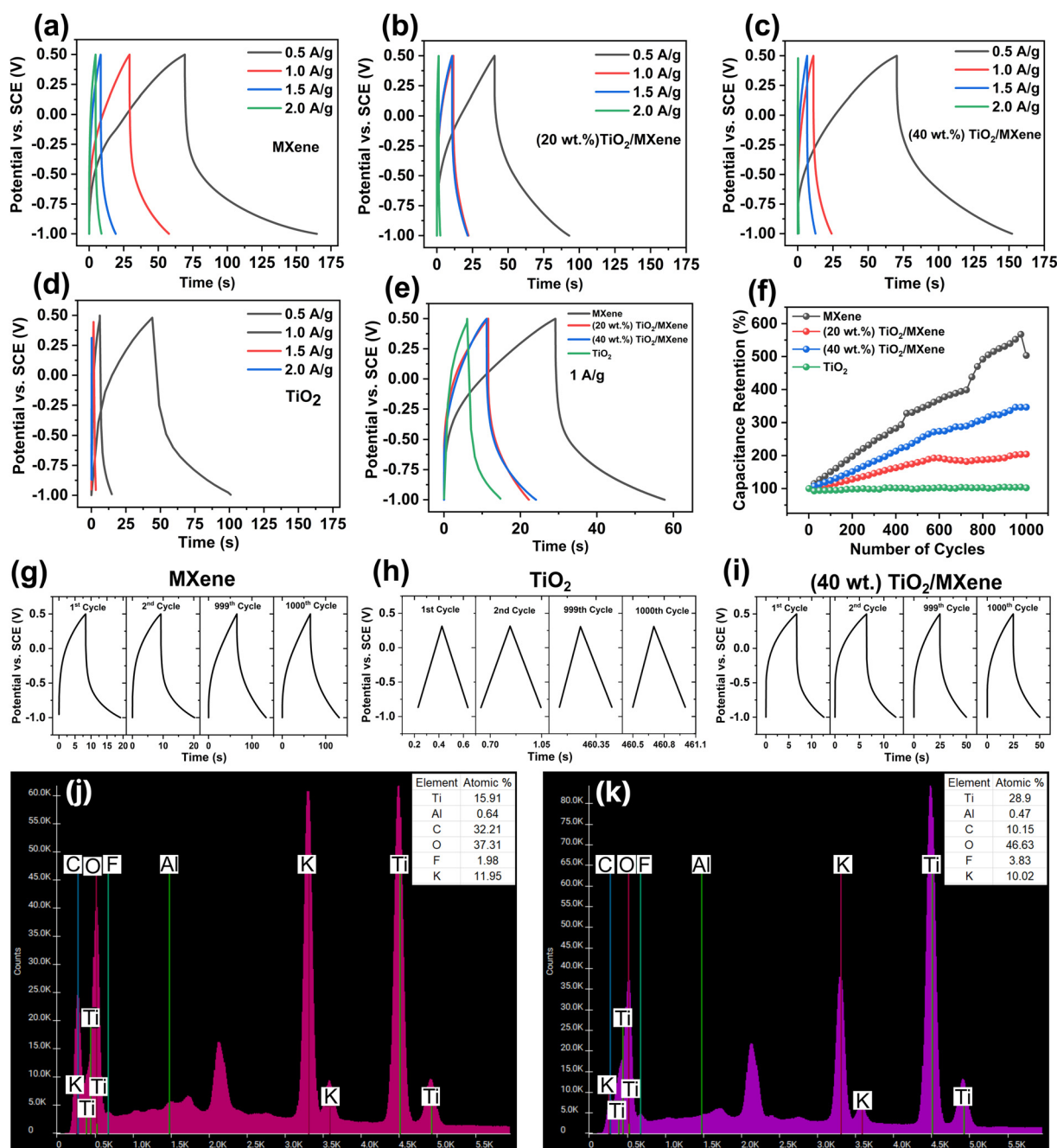


Fig. 6 The GCD data for fabricated electrodes. (a)–(d) at multiple current densities; (e) at a  $1\ A\ g^{-1}$  constant current density; (f) capacitance retention graph at a  $1.5\ A\ g^{-1}$  current density; (g)–(i) potential profiles during cycling for MXene,  $TiO_2$ , and (40 wt.)  $TiO_2$ /MXene; EDS spectrum data for (j) MXene and (k) (20 wt%)  $TiO_2$ /MXene electrodes after 1000 charging–discharging cycles.



higher than  $1.16 \text{ F g}^{-1}$  at  $1.5 \text{ A g}^{-1}$ . This discrepancy is due to the poor performance of  $\text{TiO}_2$ , facilitating a decrease in the effective potential window ( $< 1.5 \text{ V}$ ). It is evident from Fig. 6(h) that the potential window for the  $\text{TiO}_2$  sample is  $\sim 1.12 \text{ V}$  as opposed to  $1.5 \text{ V}$  for all other samples. Furthermore, the specific capacitance is inversely proportional to the potential window, thereby leading to a higher calculated specific capacitance. While the MXene sample showed a 568% increase in the specific capacitance and the (20 wt%)  $\text{TiO}_2/\text{MXene}$  and (40 wt%)  $\text{TiO}_2/\text{MXene}$  nanocomposite samples exhibited 204% and 346% increases, respectively. To investigate this, EDS spectrum analysis before and after GCD tests were performed on the MXene and (20 wt%)  $\text{TiO}_2/\text{MXene}$  samples shown in Fig. 6(j) and (k).

It is evident from the intense K peaks in the EDS spectrum shown in Fig. 6(j) and (k) that  $\text{K}^+$  ions have intercalated into the structure from the 1 M KOH electrolyte solution. Additionally, the O intensity counts are significantly higher compared to F for both samples as well. To further quantify the amount of elemental modification, the atomic percentage for O, F, and K before and after GCD tests for (20 wt%)  $\text{TiO}_2/\text{MXene}$  is tabulated in Table 6. The values indicate that the atomic% of O has increased by  $\sim 24\%$ , whereas for F, it has decreased by  $\sim 34\%$ . In addition, approximately a 10 atomic% of K was present after

GCD, which was absent before. A similar phenomenon was also reported in a recent study by I. Cho *et al.*, where the MXene sample demonstrated an increase of 125% in the specific capacitance during the GCD test.<sup>57</sup> This is attributed to the intercalation of  $\text{K}^+$  ions and the substitution of the  $-\text{F}$  surface terminator group with  $-\text{OH}$  bonds. Therefore, this implies that the surface terminator group has been modified during the cycling process, facilitating a tremendous increase in the capacitance.

According to several studies, the ion intercalation and surface terminator group modification essentially enhances electronic conductivity and charge transport efficiency, hence gradually improving the specific capacitance with each cycle,<sup>58–61</sup> Although a deeper understanding of this phenomenon requires further exploration using chemical bond characterization techniques such as XPS, Raman, or FTIR spectroscopy, we have outlined two proposed mechanisms in Section 3.5, which are based on the existing literature.

Although the specific capacitance calculated from GCD and CV follows a similar decreasing trend with an increasing scan rate or current density, the values derived from GCD are consistently lower. This discrepancy arises from the fundamental difference in operating conditions and sensitivity toward the voltage drop ( $iR$ ). The CV tests are conducted at a constant potential sweep rate (or scan rate), measuring the resultant current output, elucidating the capacitive nature of the electrode material, and determining the maximum achievable capacitance. Whereas the GCD tests are conducted at a constant current, measuring the voltage across the three-electrode system. Furthermore, GCD is significantly more susceptible to a voltage drop during the discharging cycle (*i.e.*, the vertical portion in the potential vs. time plot), which stems from various other factors such as the electrode material, current collector,

**Table 6** Elemental atomic % obtained from the EDS spectrum before and after the charging–discharging tests

(20 wt%) $\text{TiO}_2/\text{MXene}$ nanocomposite	Element atomic%		
	O	F	K
Before GCD	22.52	37.34	—
After GCD	46.63	3.83	10.02

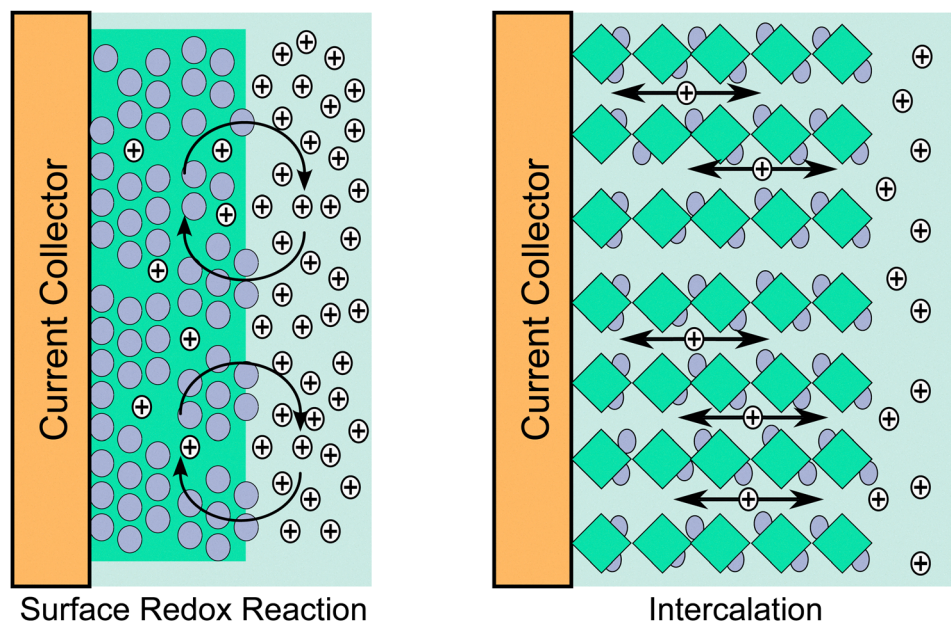


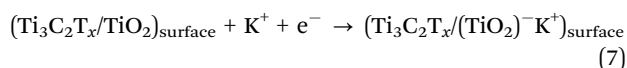
**Fig. 7** A schematic diagram illustrating the surface redox reaction and intercalation mechanisms for energy storage in pseudocapacitors.



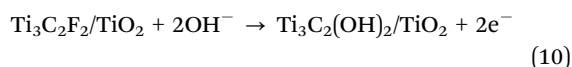
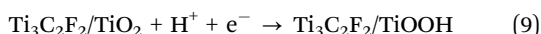
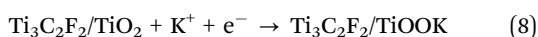
electrode–collector interface resistance, *etc.* It becomes more pronounced at higher current densities and is often unavoidable. As a result, significant distortion was observed rather than a perfect linear line in the GCD plots as can be seen in Fig. 6(a)–(d), thereby leading to a lower specific capacitance value. Nevertheless, GCD provides a realistic assessment, including the impact of the voltage drop, which helps to predict the real-world applicability of the electrode material.

### 3.5. Energy storage mechanism

Based on the existing literature, the pseudocapacitive behavior of materials involves faradaic reactions. These reactions can be explained by two proposed mechanisms: the surface redox reaction and intercalation/deintercalation of cations. A schematic illustration of the surface redox and intercalation pseudocapacitance mechanisms is given in Fig. 7. The first mechanism involves the adsorption and desorption of ions ( $K^+$ ) from the selected electrolyte (KOH) on the electrode surface and facilitates the redox reaction shown in eqn (7):<sup>62</sup>



The second mechanism is based on the intercalation of cations ( $K^+$  and  $H^+$ ) from the selected electrolyte and substitution of the  $-F$  terminator group by  $-OH$  in the MXene.<sup>57,63</sup> The proposed reactions are given in eqn (8)–(10):



## 4. Conclusions

In summary, we explored the electrochemical properties of fabricated  $TiO_2$ /MXene nanocomposites using a contemporary cold-sintering technique by employing low temperature and pressure. According to the characterization results, the sintered pellets demonstrated a rough surface morphology with more than 85% relative density. Furthermore, a quantitative relationship between the  $TiO_2$  content and the electrochemical response of the nanocomposites was established using electrochemical characterization, including cyclic voltammetry, EIS, and GCD. The cyclic voltammetry tests revealed that the (20 wt%)  $TiO_2$ /MXene and (40 wt%)  $TiO_2$ /MXene nanocomposite samples exhibit a specific capacitance of  $79.52 \text{ F g}^{-1}$  and  $117 \text{ F g}^{-1}$ , respectively, at a  $10 \text{ mV s}^{-1}$  scan rate. At a  $10 \text{ mV s}^{-1}$  scan rate, these specific capacitance values are 1.5–2 times more significant than the pristine MXene ( $55.29 \text{ F g}^{-1}$ ). The specific capacitance from single-cycle GCD tests did not follow any particular pattern, showing  $42.92 \text{ F g}^{-1}$ ,  $26.84 \text{ F g}^{-1}$ , and  $45.32 \text{ F g}^{-1}$  at a  $0.5 \text{ A g}^{-1}$  current density for the pristine MXene, (20 wt%)  $TiO_2$ /MXene and (40 wt%)  $TiO_2$ /MXene, respectively. However, more than a 200%

increase in capacitance retention was observed in the GCD tests after 1000 cycles for all the samples, attributed to the  $K^+$  intercalation and modification in the surface terminator group ( $T_x$ ) during the charging–discharging process. In addition, EIS suggests that the charge transfer improves with the addition of the  $TiO_2$  amount, reaching a resistance value as low as  $0.51 \Omega \text{ cm}^2$  for 40 wt%  $TiO_2$ . Moreover, the cold-sintering method is a novel approach to fabricating  $TiO_2$ /MXene nanocomposites, opening new avenues for further research, including the optimization of cold-sintering parameters (*e.g.*, temperature and pressure), determination of the ideal  $TiO_2$  content, and the impact of various electrolyte ions on the nanocomposite's performance.

## Author contributions

Abdul Hamid Rumman: conceptualization, data curation, formal analysis, investigation, methodology, visualization, and writing – original draft. Saimon Mahmud: conceptualization, formal analysis, investigation, methodology, and writing – original draft. Nishat Tasnim Mim: conceptualization, validation, and writing – original draft. Janifa Akter: conceptualization, validation, and writing – original draft. Ananya Roy: validation and writing – original draft. Ahsior Rahman Nirjhar: investigation and writing – review & editing. Md. Nazmul Ahsan Dipon: investigation and writing – review & editing. Md. Shofiql Islam: investigation and resources. Md. Abdul Gafur: resources, supervision, and writing – review & editing. Aninda Nafis Ahmed: resources, supervision, and writing – review & editing. Kazi Md. Shorowordi: conceptualization, project administration, resources, supervision, and writing – review & editing.

## Conflicts of interest

There are no conflicts to declare.

## Data availability

The data supporting the findings are included within the article and its ESI.†

## Acknowledgements

The authors would like to thank Dr. Umme Sarmeen Akhtar, Senior Scientific Officer, BCSIR, for her assistance with the XPS tests on the  $Ti_3AlC_2$  MAX phase and  $Ti_3C_2T_x$  samples. Additionally, the authors express their sincere gratitude to Mohd. Rakibul Hasan Abed and Miah Abdullah Sahriar for providing valuable insights and guidance during initial planning phase of the project.

## References

- 1 M. Şahin, F. Blaabjerg and A. Sangwongwanich, A Comprehensive Review on Supercapacitor Applications and



- Developments, *Energies*, 2022, **15**(3), 674, DOI: [10.3390/en15030674](https://doi.org/10.3390/en15030674).
- 2 M. Jayalakshmi and K. Balasubramanian, Simple Capacitors to Supercapacitors – An Overview, *Int. J. Electrochem. Sci.*, 2008, **3**(11), 1196–1217, DOI: [10.1016/S1452-3981\(23\)15517-9](https://doi.org/10.1016/S1452-3981(23)15517-9).
  - 3 M. V. Kiamahalleh, S. H. S. Zein, G. Najafpour, S. A. Sata and S. Buniran, Multiwalled Carbon Nanotubes Based Nanocomposites for Supercapacitors: A Review of Electrode Materials, *Nano*, 2012, **7**(2), 1230002, DOI: [10.1142/S1793292012300022](https://doi.org/10.1142/S1793292012300022).
  - 4 Z. S. Iro, C. Subramani and S. S. Dash, A Brief Review on Electrode Materials for Supercapacitor, *Int. J. Electrochem. Sci.*, 2016, **11**(12), 10628–10643, DOI: [10.20964/2016.12.50](https://doi.org/10.20964/2016.12.50).
  - 5 S. Najib and E. Erdem, Current progress achieved in novel materials for supercapacitor electrodes: mini review, *Nanoscale Adv.*, 2019, **1**(8), 2817–2827, DOI: [10.1039/C9NA00345B](https://doi.org/10.1039/C9NA00345B).
  - 6 M. Vangari, T. Pryor and L. Jiang, Supercapacitors: Review of Materials and Fabrication Methods, *J. Energy Eng.*, 2013, **139**(2), 72–79, DOI: [10.1061/\(ASCE\)EY.1943-7897.0000102](https://doi.org/10.1061/(ASCE)EY.1943-7897.0000102).
  - 7 Y. Jiang and J. Liu, Definitions of Pseudocapacitive Materials: A Brief Review, *Energy Environ. Mater.*, 2019, **2**(1), 30–37, DOI: [10.1002/eem2.12028](https://doi.org/10.1002/eem2.12028).
  - 8 B. Anasori, M. R. Lukatskaya and Y. Gogotsi, 2D metal carbides and nitrides (MXenes) for energy storage, *Nat. Rev. Mater.*, 2017, **2**(2), 16098, DOI: [10.1038/natrevmats.2016.98](https://doi.org/10.1038/natrevmats.2016.98).
  - 9 T. Kar, S. Godavarthi, S. K. Pasha, K. Deshmukh, L. Martínez-Gómez and M. K. Kesarla, Layered materials and their heterojunctions for supercapacitor applications: a review, *Crit. Rev. Solid State Mater. Sci.*, 2022, **47**(3), 357–388, DOI: [10.1080/10408436.2021.1886048](https://doi.org/10.1080/10408436.2021.1886048).
  - 10 P. Forouzandeh and S. C. Pillai, MXenes-based nanocomposites for supercapacitor applications, *Curr. Opin. Chem. Eng.*, 2021, **33**, 100710, DOI: [10.1016/j.coche.2021.100710](https://doi.org/10.1016/j.coche.2021.100710).
  - 11 Y. Dai, C. Sun, H. Gul, L. Tan, Y. Guo, D. Qiu, Y. Gu, Y. Chen, C. Ge, D. Huang, B. Chen, J. Hua and J. Zhao, Three-dimensional honeycomb composites consist of metal carbides and layered double hydroxides for high-performance supercapacitor electrode materials, *J. Power Sources*, 2024, **602**, 234306, DOI: [10.1016/j.jpowsour.2024.234306](https://doi.org/10.1016/j.jpowsour.2024.234306).
  - 12 Y. Yu, H. Zhang, Y. Xie, F. Jiang, X. Gao, H. Bai, F. Yao and H. Yue, Vertically aligned graphene-MXene nanosheets based electrodes for high electrochemical performance asymmetric supercapacitor, *Chem. Eng. J.*, 2024, **482**, 149063, DOI: [10.1016/j.cej.2024.149063](https://doi.org/10.1016/j.cej.2024.149063).
  - 13 X. Liang, Y. Chen, Z. Jiao, M. Demir, M. Du and J. Han, MXene-transition metal sulfide composite electrodes for supercapacitors: Synthesis and electrochemical characterization, *J. Energy Storage*, 2024, **88**, 111634, DOI: [10.1016/j.est.2024.111634](https://doi.org/10.1016/j.est.2024.111634).
  - 14 L. Wang, S. Zhao, X. Zhang, Y. Xu, Y. An, C. Li, S. Yi, C. Liu, K. Wang, X. Sun, H. Zhang and Y. Ma, *In Situ* Construction of Bimetallic Selenides Heterogeneous Interface on Oxidation-Stable  $Ti_3C_2T_x$  MXene Toward Lithium Storage with Ultrafast Charge Transfer Kinetics, *Small*, 2024, **20**(48), DOI: [10.1002/smll.202403078](https://doi.org/10.1002/smll.202403078).
  - 15 B. Gao, X. Li, Y. Ma, Y. Cao, Z. Hu, X. Zhang, J. Fu, K. Huo and P. K. Chu,  $MnO_2$ - $TiO_2/C$  nanocomposite arrays for high-performance supercapacitor electrodes, *Thin Solid Films*, 2015, **584**, 61–65, DOI: [10.1016/j.tsf.2014.09.071](https://doi.org/10.1016/j.tsf.2014.09.071).
  - 16 M. Zhao, C. E. Ren, Z. Ling, M. R. Lukatskaya, C. Zhang, K. L. V. Aken, M. W. Barsoum and Y. Gogotsi, Flexible MXene/Carbon Nanotube Composite Paper with High Volumetric Capacitance, *Adv. Mater.*, 2015, **27**(2), 339–345, DOI: [10.1002/adma.201404140](https://doi.org/10.1002/adma.201404140).
  - 17 M. Sawczak, M. Sobaszek, K. Siuzdak, J. Ryl, R. Bogdanowicz, K. Darowicki, M. Gazda and A. Cenian, Formation of Highly Conductive Boron-Doped Diamond on  $TiO_2$  Nanotubes Composite for Supercapacitor or Energy Storage Devices, *J. Electrochem. Soc.*, 2015, **162**(10), A2085–A2092, DOI: [10.1149/2.0551510jes](https://doi.org/10.1149/2.0551510jes).
  - 18 Y. Gao, L. Wang, A. Zhou, Z. Li, J. Chen, H. Bala, Q. Hu and X. Cao, Hydrothermal synthesis of  $TiO_2/Ti_3C_2$  nanocomposites with enhanced photocatalytic activity, *Mater. Lett.*, 2015, **150**, 62–64, DOI: [10.1016/j.matlet.2015.02.135](https://doi.org/10.1016/j.matlet.2015.02.135).
  - 19 Q. Jiang, N. Kurra, M. Alhabeab, Y. Gogotsi and H. N. Alshareef, All Pseudocapacitive MXene- $RuO_2$  Asymmetric Supercapacitors, *Adv. Energy Mater.*, 2018, **8**, 13, DOI: [10.1002/aenm.201703043](https://doi.org/10.1002/aenm.201703043).
  - 20 J. Zhu, Y. Tang, C. Yang, F. Wang and M. Cao, Composites of  $TiO_2$  Nanoparticles Deposited on  $Ti_3C_2$  MXene Nanosheets with Enhanced Electrochemical Performance, *J. Electrochem. Soc.*, 2016, **163**(5), A785–A791, DOI: [10.1149/2.0981605jes](https://doi.org/10.1149/2.0981605jes).
  - 21 K. Xie, J. Wang, K. Xu, Z. Wei, M. Zhang and J. Zhang, *In situ* synthesis of fluorine-free MXene/ $TiO_2$  composite for high-performance supercapacitor, *Arabian J. Chem.*, 2024, **17**(2), 105551, DOI: [10.1016/j.arabjc.2023.105551](https://doi.org/10.1016/j.arabjc.2023.105551).
  - 22 B. Ahmed, D. H. Anjum, M. N. Hedhili, Y. Gogotsi and H. N. Alshareef,  $H_2O_2$  assisted room temperature oxidation of  $Ti_2C$  MXene for Li-ion battery anodes, *Nanoscale*, 2016, **8**(14), 7580–7587, DOI: [10.1039/C6NR00002A](https://doi.org/10.1039/C6NR00002A).
  - 23 M. Noman, M. M. Baig, Q. M. Saqib, S. R. Patil, C. S. Patil, J. Kim, Y. Ko, E. Lee, J. Hwang, S. G. Lee and J. Bae,  $Ti_3C_2T_x$ -MXene based 2D/3D  $Ti_3C_2$ - $TiO_2$ - $CuTiO_3$  heterostructure for enhanced pseudocapacitive performance, *Chem. Eng. J.*, 2024, **499**, 156697, DOI: [10.1016/j.cej.2024.156697](https://doi.org/10.1016/j.cej.2024.156697).
  - 24 B. E. Watt, A. T. Proudfoot and J. A. Vale, Hydrogen Peroxide Poisoning, *Toxicol. Rev.*, 2004, **23**(1), 51–57, DOI: [10.2165/00139709-200423010-00006](https://doi.org/10.2165/00139709-200423010-00006).
  - 25 M. Naguib, O. Mashtalir, M. R. Lukatskaya, B. Dyatkin, C. Zhang, V. Presser, Y. Gogotsi and M. W. Barsoum, One-step synthesis of nanocrystalline transition metal oxides on thin sheets of disordered graphitic carbon by oxidation of MXenes, *Chem. Commun.*, 2014, **50**(56), 7420–7423, DOI: [10.1039/C4CC01646G](https://doi.org/10.1039/C4CC01646G).
  - 26 J. Hong, C. Paeng, S. Park, I. In, H. Lee, N. B. Velhal, T. H. Yun, C. Jo and C. Yim, Flashlight treatment for instantaneous structuring of dense MXene film into porous MXene/ $TiO_2$  nanocomposite for lithium-ion battery anodes, *Chem. Eng. J.*, 2024, **484**, 149598, DOI: [10.1016/j.cej.2024.149598](https://doi.org/10.1016/j.cej.2024.149598).
  - 27 R. B. Rakhi, B. Ahmed, M. N. Hedhili, D. H. Anjum and H. N. Alshareef, Effect of Postetch Annealing Gas Composition on



- the Structural and Electrochemical Properties of  $\text{Ti}_2\text{CT}_x$  MXene Electrodes for Supercapacitor Applications, *Chem. Mater.*, 2015, 27(15), 5314–5323, DOI: [10.1021/acs.chemmater.5b01623](https://doi.org/10.1021/acs.chemmater.5b01623).
- 28 A. Galotta and V. M. Sglavo, The cold sintering process: A review on processing features, densification mechanisms and perspectives, *J. Eur. Ceram. Soc.*, 2021, 41(16), 1–17, DOI: [10.1016/j.jeurceramsoc.2021.09.024](https://doi.org/10.1016/j.jeurceramsoc.2021.09.024).
- 29 J. Guo, B. Legum, B. Anasori, K. Wang, P. Lelyukh, Y. Gogotsi and C. A. Randall, Cold Sintered Ceramic Nanocomposites of 2D MXene and Zinc Oxide, *Adv. Mater.*, 2018, 30, 32, DOI: [10.1002/adma.201801846](https://doi.org/10.1002/adma.201801846).
- 30 T. Theivasanthi, *Review on Titania Nanopowder- Processing and Applications*, arXiv, 2017, preprint, arXiv:1704.00981, DOI: [10.48550/1704.00981](https://doi.org/10.48550/1704.00981).
- 31 W. Zhou, B. Mei, J. Zhu and X. Hong, Synthesis of high-purity  $\text{Ti}_3\text{SiC}_2$  and  $\text{Ti}_3\text{AlC}_2$  by spark plasma sintering (SPS) technique, *J. Mater. Sci.*, 2005, 40(8), 2099–2100, DOI: [10.1007/s10853-005-1245-z](https://doi.org/10.1007/s10853-005-1245-z).
- 32 A. Hendaoui, D. Vrel, A. Amara, A. Benaldjia and P. Langlois, Ti–Al–C MAX phases by aluminothermic reduction process, *Int. J. Self-Propag. High-Temp. Synth.*, 2008, 17(2), 125–128, DOI: [10.3103/S1061386208020076](https://doi.org/10.3103/S1061386208020076).
- 33 A. Zhou, C.-A. Wang and Y. Hunag, Synthesis and mechanical properties of  $\text{Ti}_3\text{AlC}_2$  by spark plasma sintering, *J. Mater. Sci.*, 2003, 38(14), 3111–3115, DOI: [10.1023/A:1024777213910](https://doi.org/10.1023/A:1024777213910).
- 34 W. Hong, B. C. Wyatt, S. K. Nemani and B. Anasori, Double transition-metal MXenes: Atomistic design of two-dimensional carbides and nitrides, *MRS Bull.*, 2020, 45(10), 850–861, DOI: [10.1557/mrs.2020.251](https://doi.org/10.1557/mrs.2020.251).
- 35 A. Ghosh, H. Pal, T. Das, S. Chatterjee and A. Das, Synthesis and Characterization of MXene from MAX phase, *Mater. Today: Proc.*, 2022, 58, 714–716, DOI: [10.1016/j.matpr.2022.02.253](https://doi.org/10.1016/j.matpr.2022.02.253).
- 36 Y. Wei, P. Zhang, R. A. Soomro, Q. Zhu and B. Xu, Advances in the Synthesis of 2D MXenes, *Adv. Mater.*, 2021, 33(39), 2103148, DOI: [10.1002/adma.202103148](https://doi.org/10.1002/adma.202103148).
- 37 M. Alhabeab, K. Maleski, B. Anasori, P. Lelyukh, L. Clark, S. Sin and Y. Gogotsi, Guidelines for Synthesis and Processing of Two-Dimensional Titanium Carbide ( $\text{Ti}_3\text{C}_2\text{T}_x$  MXene), *Chem. Mater.*, 2017, 29(18), 7633–7644, DOI: [10.1021/acs.chemmater.7b02847](https://doi.org/10.1021/acs.chemmater.7b02847).
- 38 L.-Å. Näslund, P. O. Å. Persson and J. Rosen, X-ray Photoelectron Spectroscopy of  $\text{Ti}_3\text{AlC}_2$ ,  $\text{Ti}_3\text{C}_2\text{T}_2$ , and TiC Provides Evidence for the Electrostatic Interaction between Laminated Layers in MAX-Phase Materials, *J. Phys. Chem. C*, 2020, 124(50), 27732–27742, DOI: [10.1021/acs.jpcc.0c07413](https://doi.org/10.1021/acs.jpcc.0c07413).
- 39 S. Munir, A. Rasheed, T. Rasheed, I. Ayman, S. Ajmal, A. Rehman, I. Shakir, P. O. Agboola and M. F. Warsi, Exploring the Influence of Critical Parameters for the Effective Synthesis of High-Quality 2D MXene, *ACS Omega*, 2020, 5(41), 26845–26854, DOI: [10.1021/acsomega.0c03970](https://doi.org/10.1021/acsomega.0c03970).
- 40 J. Jimmy and B. Kandasubramanian, Mxene functionalized polymer composites: Synthesis and applications, *Eur. Polym. J.*, 2020, 122, 109367, DOI: [10.1016/j.eurpolymj.2019.109367](https://doi.org/10.1016/j.eurpolymj.2019.109367).
- 41 B. Scheibe, V. Kupka, B. Peplińska, M. Jarek and K. Tadyszak, The Influence of Oxygen Concentration during MAX Phases ( $\text{Ti}_3\text{AlC}_2$ ) Preparation on the  $\alpha\text{-Al}_2\text{O}_3$  Microparticles Content and Specific Surface Area of Multilayered MXenes ( $\text{Ti}_3\text{C}_2\text{T}_x$ ), *Materials*, 2019, 12(3), 353, DOI: [10.3390/ma12030353](https://doi.org/10.3390/ma12030353).
- 42 W. Peng, R. Hu, W. Jiang, J. Kang, J. Li, Y. Cao and M. Xiang, Effects of MXene on Nonisothermal Crystallization Kinetics of Isotactic Polypropylene, *ACS Omega*, 2021, 6(30), 19973–19982, DOI: [10.1021/acsomega.1c02970](https://doi.org/10.1021/acsomega.1c02970).
- 43 G. Sharma, M. Naguib, D. Feng, Y. Gogotsi and A. Navrotsky, Calorimetric Determination of Thermodynamic Stability of MAX and MXene Phases, *J. Phys. Chem. C*, 2016, 120(49), 28131–28137, DOI: [10.1021/acs.jpcc.6b10241](https://doi.org/10.1021/acs.jpcc.6b10241).
- 44 L. R. De Jesús Báez, A. S. Rosas, P. Mahale and T. E. Mallouk, Chelation-Based Route to Aluminum-Free Layered Transition Metal Carbides (MXenes), *ACS Omega*, 2023, 8(44), 41969–41976, DOI: [10.1021/acsomega.3c07442](https://doi.org/10.1021/acsomega.3c07442).
- 45 A. Vittadini, F. Sedona, S. Agnoli, L. Artiglia, M. Casarin, G. A. Rizzi, M. Sambri and G. Granozzi, Stability of  $\text{TiO}_2$  Polymorphs: Exploring the Extreme Frontier of the Nanoscale, *ChemPhysChem*, 2010, 11(7), 1550–1557, DOI: [10.1002/cphc.200900872](https://doi.org/10.1002/cphc.200900872).
- 46 S. Z. Abbas, D. Vikraman, Z. A. Sheikh, S. Ali, I. Hussain, J. C. Goak, H. S. Kim, D. Byun, J. Jung, S. Hussain and N. Lee, Improving the electrochemical properties of MXene through intercalation of WC and TiC nanoparticles for supercapacitors application, *J. Colloid Interface Sci.*, 2025, 696, 137845, DOI: [10.1016/j.jcis.2025.137845](https://doi.org/10.1016/j.jcis.2025.137845).
- 47 B. P. Thapaliya, C. J. Jafta, H. Lyu, J. Xia, H. M. Meyer III, M. P. Paranthaman, X. Sun, C. A. Bridges and S. Dai, Fluorination of MXene by Elemental F<sub>2</sub> as Electrode Material for Lithium-Ion Batteries, *ChemSusChem*, 2019, 12(7), 1316–1324, DOI: [10.1002/cssc.201900003](https://doi.org/10.1002/cssc.201900003).
- 48 Y. Dall'Agnese, M. R. Lukatskaya, K. M. Cook, P.-L. Taberna, Y. Gogotsi and P. Simon, High capacitance of surface-modified 2D titanium carbide in acidic electrolyte, *Electrochem. Commun.*, 2014, 48, 118–122, DOI: [10.1016/j.elecom.2014.09.002](https://doi.org/10.1016/j.elecom.2014.09.002).
- 49 Y.-K. Paek, C.-K. Shin, K.-S. Oh, T.-J. Chung and H. J. Cho, Low-temperature Sintering Behavior of  $\text{TiO}_2$  Activated with CuO, *J. Korean Ceram. Soc.*, 2016, 53(6), 682–688, DOI: [10.4191/kcers.2016.53.6.682](https://doi.org/10.4191/kcers.2016.53.6.682).
- 50 J. Yan, C. E. Ren, K. Maleski, C. B. Hatter, B. Anasori, P. Urbankowski, A. Sarycheva and Y. Gogotsi, Flexible MXene/Graphene Films for Ultrafast Supercapacitors with Outstanding Volumetric Capacitance, *Adv. Funct. Mater.*, 2017, 27(30), DOI: [10.1002/adfm.201701264](https://doi.org/10.1002/adfm.201701264).
- 51 Y. Gogotsi and R. M. Penner, Energy Storage in Nanomaterials – Capacitive, Pseudocapacitive, or Battery-like?, *ACS Nano*, 2018, 12(3), 2081–2083, DOI: [10.1021/acsnano.8b01914](https://doi.org/10.1021/acsnano.8b01914).
- 52 Z. K. Ghouri, N. A. M. Barakat and H. Y. Kim, Synthesis and Electrochemical Properties of  $\text{MnO}_2$  and Co-Decorated Graphene as Novel Nanocomposite for Electrochemical Super Capacitors Application, *Energy Environ. Focus*, 2015, 4(1), 34–39, DOI: [10.1166/eef.2015.1136](https://doi.org/10.1166/eef.2015.1136).
- 53 A. Ch Lazanas and M. I. Prodromidis, Electrochemical Impedance Spectroscopy—A Tutorial, *ACS Meas. Sci. Au*, 2023, 3(3), 162–193, DOI: [10.1021/acsmeasuresciau.2c00070](https://doi.org/10.1021/acsmeasuresciau.2c00070).



- 54 S. M. Gateman, O. Gharbi, H. Gomes de Melo, K. Ngo, M. Turmine and V. Vivier, On the use of a constant phase element (CPE) in electrochemistry, *Curr. Opin. Electrochem.*, 2022, **36**, 101133, DOI: [10.1016/j.coelec.2022.101133](https://doi.org/10.1016/j.coelec.2022.101133).
- 55 A. Lasia, The Origin of the Constant Phase Element, *J. Phys. Chem. Lett.*, 2022, **13**(2), 580–589, DOI: [10.1021/acs.jpclett.1c03782](https://doi.org/10.1021/acs.jpclett.1c03782).
- 56 W. Shaheen, M. F. Warsi, M. Shahid, M. A. Khan, M. Asghar, Z. Ali, M. Sarfraz, H. Anwar, M. Nadeem and I. Shakir, Carbon Coated MoO<sub>3</sub> Nanowires/Graphene oxide Ternary Nanocomposite for High-Performance Supercapacitors, *Electrochim. Acta*, 2016, **219**, 330–338, DOI: [10.1016/j.electacta.2016.09.069](https://doi.org/10.1016/j.electacta.2016.09.069).
- 57 I. Cho, A. R. Selvaraj, J. Bak, H. Kim and K. Prabakar, Anomalous increase in specific capacitance in MXene during galvanostatic cycling studies, *J. Energy Storage*, 2022, **53**, 105207, DOI: [10.1016/j.est.2022.105207](https://doi.org/10.1016/j.est.2022.105207).
- 58 T. Schultz, N. C. Frey, K. Hantanasirisakul, S. Park, S. J. May, V. B. Shenoy, Y. Gogotsi and N. Koch, Surface Termination Dependent Work Function and Electronic Properties of Ti<sub>3</sub>C<sub>2</sub>T<sub>x</sub> MXene, *Chem. Mater.*, 2019, **31**(17), 6590–6597, DOI: [10.1021/acs.chemmater.9b00414](https://doi.org/10.1021/acs.chemmater.9b00414).
- 59 J. Li, Y. Liu, J. Hu, N. Chen, G. Du and C. Jiang, K + Intercalation of NH<sub>4</sub>HF<sub>2</sub>-Exfoliated Ti<sub>3</sub>C<sub>2</sub> MXene as Binder-Free Electrodes with High Electrochemical Capacitance, *Phys. Status Solidi A*, 2020, **217**(8), DOI: [10.1002/pssa.201900806](https://doi.org/10.1002/pssa.201900806).
- 60 M. Khazaei, M. Arai, T. Sasaki, A. Ranjbar, Y. Liang and S. Yunoki, OH-terminated two-dimensional transition metal carbides and nitrides as ultralow work function materials, *Phys. Rev. B: Condens. Matter Mater. Phys.*, 2015, **92**(7), 075411, DOI: [10.1103/PhysRevB.92.075411](https://doi.org/10.1103/PhysRevB.92.075411).
- 61 J. L. Hart, K. Hantanasirisakul, A. C. Lang, B. Anasori, D. Pinto, Y. Pivak, J. T. v. Ommé, S. J. May, Y. Gogotsi and M. L. Taheri, Control of MXenes' electronic properties through termination and intercalation, *Nat. Commun.*, 2019, **10**(1), 522, DOI: [10.1038/s41467-018-08169-8](https://doi.org/10.1038/s41467-018-08169-8).
- 62 M. Mahmood, A. Rasheed, I. Ayman, T. Rasheed, S. Munir, S. Ajmal, P. O. Agboola, M. F. Warsi and M. Shahid, Synthesis of Ultrathin MnO<sub>2</sub> Nanowire-Intercalated 2D-MXenes for High-Performance Hybrid Supercapacitors, *Energy Fuels*, 2021, **35**(4), 3469–3478, DOI: [10.1021/acs.energyfuels.0c03939](https://doi.org/10.1021/acs.energyfuels.0c03939).
- 63 H. Zhou, Y. Lu, F. Wu, L. Fang, H. Luo, Y. Zhang and M. Zhou, MnO<sub>2</sub> nanorods/MXene/CC composite electrode for flexible supercapacitors with enhanced electrochemical performance, *J. Alloys Compd.*, 2019, **802**, 259–268, DOI: [10.1016/j.jallcom.2019.06.173](https://doi.org/10.1016/j.jallcom.2019.06.173).

